Superresolution imaging reveals activity-dependent plasticity of axon morphology linked to changes in action potential conduction velocity

Ronan Chéreau[a,b], G. Ezequiel Saraceno[a,b], Julie Angibaud[a,b], Daniel Cattaert[a,c], and U. Valentin Nägerl[a,b,1]

[a]Department of Life and Health Sciences, Université de Bordeaux, 33077 Bordeaux, France; [b]Interdisciplinary Institute for Neuroscience, UMR 5297, Centre National de la Recherche Scientifique, 33077 Bordeaux, France; and [c]Institut de Neurosciences Cognitives et Intégratives d'Aquitaine, UMR 5287, Centre National de Recherche Scientifique, 33077 Bordeaux, France

Edited by Jeff W. Lichtman, Harvard University, Cambridge, MA, and approved December 23, 2016 (received for review May 12, 2016)

Axons convey information to nearby and distant cells, and the time it takes for action potentials (APs) to reach their targets governs the timing of information transfer in neural circuits. In the unmyelinated axons of hippocampus, the conduction speed of APs depends crucially on axon diameters, which vary widely. However, it is not known whether axon diameters are dynamic and regulated by activity-dependent mechanisms. Using time-lapse superresolution microscopy in brain slices, we report that axons grow wider after high-frequency AP firing: synaptic boutons undergo a rapid enlargement, which is mostly transient, whereas axon shafts show a more delayed and progressive increase in diameter. Simulations of AP propagation incorporating these morphological dynamics predicted bidirectional effects on AP conduction speed. The predictions were confirmed by electrophysiological experiments, revealing a phase of slowed down AP conduction, which is linked to the transient enlargement of the synaptic boutons, followed by a sustained increase in conduction speed that accompanies the axon shaft widening induced by high-frequency AP firing. Taken together, our study outlines a morphological plasticity mechanism for dynamically fine-tuning AP conduction velocity, which potentially has wide implications for the temporal transfer of information in the brain.

STED microscopy | axons | synaptic boutons | action potential conduction velocity | plasticity

Axons have long been considered to be static transmission cables, serving to faithfully transmit all-or-none action potentials (APs) over long distances. However, several studies have revealed during the last few years that axon physiology is highly dynamic and regulated (1). It was shown that axons are capable of analog computations (2), undergo activity-dependent structural changes affecting the axonal initial segment (3) and boutons (4), and are subject to local control by astrocytes (5). As these mechanisms can substantially influence AP signaling and synaptic transmission, the computational capability and role of axons in neural circuit function are more complex than previously thought.

The conduction of AP along axons imposes widely varying delays on synaptic transmission, and hence shapes the dynamics and timing of signal processing in the brain. In unmyelinated axons, the conduction speed of AP depends crucially on axon diameters (6, 7), which typically vary along the same axon (8), as well as between axons from different cell types (9). However, it is unknown whether axon diameters are dynamic and regulated by activity-dependent mechanisms, which could affect the timing of information transfer between cells and brain areas. This knowledge gap is mostly a result of the inability of conventional light microscopy to resolve thin unmyelinated axons, which can have diameters well below 200 nm, according to electron microscopy studies (10, 11).

To overcome this limitation, we applied stimulated emission depletion (STED) microscopy together with electrophysiology in brain slices, allowing us to visualize the morphological dynamics of axons and carry out functional experiments in tandem. Numerical simulations complemented the experimental strategy.

Focusing on the classic hippocampal CA3-CA1 pathway, we observed that synaptic boutons and axon shafts enlarged after high-frequency AP firing. Whereas the boutons showed a rapid expansion, which was mostly transient, the intervening axon shafts reacted more slowly, growing gradually wider over the duration of the experiment (~1 h). On the basis of numerical simulations incorporating the amplitude and time course of these morphological dynamics, we predicted bidirectional functional effects on the conduction velocity of APs, which were confirmed by electrophysiological experiments.

Our study outlines a mechanism for fine-tuning the timing of information transfer in neural circuits, where activity-dependent changes in nanoscale axon morphology modify the conduction velocity of APs along unmyelinated axon fibers of CA3 pyramidal neurons in the hippocampus, revealing a new layer of complexity for the dynamic regulation of axon physiology.

Results

Activity-Dependent Enlargement of Synaptic Boutons and Axon Shafts. We adapted a custom-built STED microscope for live-cell imaging of GFP-labeled axons in organotypic brain slices, using an oil objective, providing a spatial resolution of around 50 nm close to the coverslip (<10 μm; *SI Appendix*, Fig. S1). This approach (Fig. 1 *A*–*C*) revealed a large morphological diversity for axons of CA3 pyramidal neurons [median axon diameter = 203 nm (range = 58–446 nm; n = 26,574 measurements over ~550 μm axon length, excluding boutons; R^2 = 0.99, from 63 axon segments and 14 slices;

Significance

Recent work has called into question the classic view of axons as electroanatomical cables that faithfully transmit nerve impulses in an all-or-none fashion over variable distances. Because of their small size, below the diffraction barrier of light microscopy, it has not been possible to resolve their dynamic morphology in living brain tissue. Enabled by a combination of live-cell superresolution stimulated emission depletion (STED) microscopy, electrophysiology, and mathematical modeling, we show here that high-frequency action potential firing induces structural enlargement of boutons and axon shafts in hippocampal brain slices, which in turn drives changes in the conduction velocity of nerve impulses (action potentials). The findings reveal a mechanism for tuning the timing of communication between nerve cells.

Author contributions: R.C. and U.V.N. designed research; R.C., G.E.S., and J.A. performed research; D.C. contributed new analytic tools; R.C., G.E.S., J.A., D.C., and U.V.N. analyzed data; and R.C. and U.V.N. wrote the paper.

The authors declare no conflict of interest.

This article is a PNAS Direct Submission.

[1]To whom correspondence should be addressed. Email: valentin.nagerl@u-bordeaux.fr.

This article contains supporting information online at www.pnas.org/lookup/suppl/doi:10.1073/pnas.1607541114/-/DCSupplemental.

NEUROSCIENCE

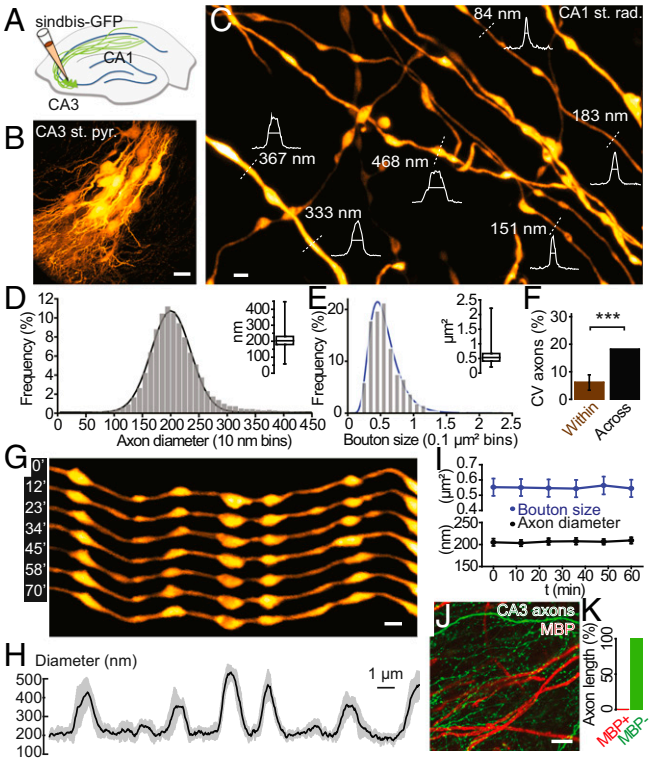

Fig. 1. Heterogeneity and dynamics of CA3 axons. (*A*) Labeling strategy. (*B*) CA3 area ∼36 h after virus injection, showing a cluster of GFP-positive pyramidal neurons. (*C*) STED image of axons in the *stratum radiatum* in the CA1 area. Intensity profiles (white) and FWHM measurements (straight lines) of axon and bouton diameters were taken at the locations indicated by the white dotted lines for illustrative purposes. (*D*) Distribution of axon diameters. Curved line is a Gaussian fit. Inset shows median value and interquartile and 0.01–99.9% range. (*E*) Distribution of synaptic bouton sizes (area). Inset shows median value and interquartile and range. (*F*) Coefficient of variations of 52 axon segment diameters within and across individual measurements. (*G*) Example of an axon segment imaged over more than 1 h. (*H*) Temporal profile of axon diameter, showing average diameter (black) and SD over time (gray). (*I*) Time-lapse data of morphological parameters over 1 h (geometric mean with 95% confidence interval), showing no alterations induced by the imaging. (*J* and *K*) Myelin basic protein immunostaining (red) showing no colocalization of the myelin with GFP-labeled CA3 axons (green) in CA1 *stratum radiatum*. Representative image (*J*) and quantification showing that more than 99.5% of total axon length is unmyelinated (*K*). [Scale bars, 20 µm (*B*), 1 µm (*C* and *G*), 10 µm (*J*).]

Fig. 1*D*); median bouton size area = 0.53 µm^2 (range = 0.2–2.2 µm^2; n = 319 synaptic boutons; R^2 = 0.98, from 63 axon segments and 14 slices; Fig. 1*E*); see *SI Appendix*, Fig. S2 for details on morphometric analysis], in agreement with previous measurements based on electron microscopy (10). Axon diameters varied more across than within axon segments (CV_{across} = 18.1%; CV_{within} = 6.1 ± 2.8%; $P < 0.001$; n = 52 axon segments from 24 slices; one sample t test; Fig. 1*F*), which may reflect consistent size differences between individual axons.

Time-lapse STED imaging showed that axons were largely stable during baseline conditions [for axon diameters, $P > 0.54$ (n = 113 individual 1-µm-long segments); for boutons, $P > 0.40$ (n = 63 boutons from five slices); Kruskal-Wallis tests; Fig. 1 *G–I*], in line with previous reports based on conventional light microscopy (4, 12).

Confocal image analysis of myelin basic protein immunostaining revealed that the vast majority of GFP-labeled CA3 axons were unmyelinated in the CA1 and CA3 areas (myelin basic protein-positive fraction: 0.08 ± 0.07%, from three slices; Fig. 1 *J* and *K* and *SI Appendix*, Fig. S3), which is consistent with previous reports in the literature (11, 13).

To test whether axon morphology can be regulated by neuronal activity, we applied high-frequency electrical stimulation (HFS) to the area of labeled CA3 neurons. Shortly after stimulation, synaptic boutons were enlarged relative to baseline levels (at 2 min: +20.7 ± 3.0% corresponding to a ∼33% increase in bouton volume; $P <$ 0.001; n = 147 boutons from five slices; one-way ANOVA; Fig. 2 *A* and *B*). However, this enlargement was mostly transient, decaying within minutes to slightly above baseline levels [at 8 min: +10.1 ± 2.5% (P = 0.006); at 14 min: +4.3 ± 2.4% (P = 0.72); Fig. 2*B*].

In contrast, axon diameters did not exhibit any statistically significant structural changes during the same period after HFS (at 2 min: +0.4 ± 1.9%; at 14 min: +3.6 ± 1.9%; $P > 0.37$; n = 148 1-µm-long shaft segments; Fig. 2 *A* and *C*).

We then patched individual CA3 pyramidal neurons with Atto 488 dye in the patch pipette (*SI Appendix*, Fig. S4*A*) and measured the structural changes in boutons in response to APs elicited by brief current injections in whole-cell current clamp mode. Confocal image analysis showed that AP firing led to a rapid enlargement of bouton size (1 min after the stimulation: +12.3 ± 3.2%; $P < 0.001$; *SI Appendix*, Fig. S4 *B* and *C*), which increased with the number of elicited APs (R^2 = 0.4; *SI Appendix*, Fig. S4 *D* and *E*). In the presence of cadmium in the bath solution (Cd^{2+}; 100 µM), which blocks voltage-gated Ca^{2+} entry and synaptic release, the bouton changes were suppressed, even though AP firing was unaffected (−0.9 ± 1.1%; $P > 0.79$; *SI Appendix*, Fig. S4 *F* and *G*).

To evaluate the persistence of the structural changes in boutons and axon shafts, we carried out additional STED time-lapse imaging experiments over a longer period (up to 60 min in total;

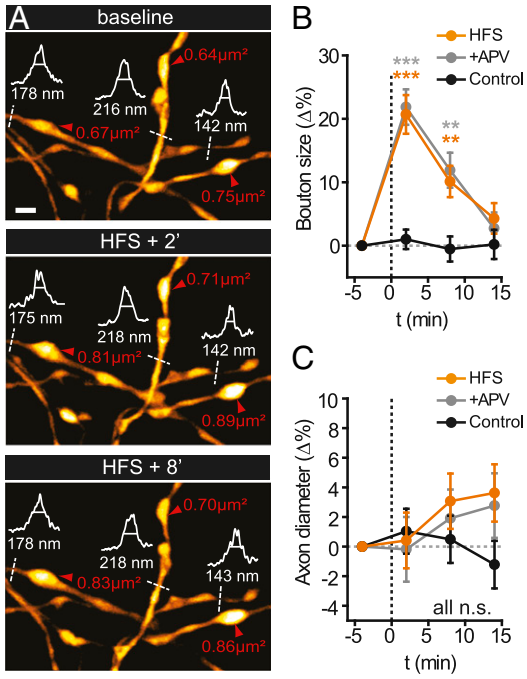

Fig. 2. STED imaging of short-term dynamics of axonal morphology. (*A*) Synaptic boutons rapidly enlarged relative to pre-HFS baseline levels (red arrowheads), whereas axon diameters remained unchanged initially (white curve, intensity profiles; dashed lines, FWHM). (*B* and *C*) Quantification of early morphological changes. (*B*) Synaptic boutons enlarged rapidly and mostly transiently after HFS (orange), whereas this effect was not blocked by APV (gray), and boutons remained stable during control conditions (black). (*C*) From the same axon segments, no significant changes in axon diameter were observed in this time frame. (Scale bar, 1 µm.)

Fig. 3*A*). Although bouton size remained slightly above baseline levels until the end of the observation period (at 45 min: +5.6 ± 1.4%; $P < 0.001$; Fig. 3*B*), axon shafts increased gradually over tens of minutes (at 33 min: +4.3 ± 0.9%; at 45 min: +5.2 ± 0.7%; $P < 0.001$; Fig. 3*C*). Moreover, HFS induced robust long-term potentiation (LTP) at CA3/CA1 synapses (+65 ± 16%; $P < 0.001$; 30–40 min after HFS; $n = 8$ slices; two-sample t test; Fig. 3*D*; recorded concurrently with the experiments shown in Fig. 3 *B* and *C*). In control experiments (without HFS), neither structure showed any significant size changes (Figs. 2 *B* and *C* and 3 *B* and *C*).

Importantly, these average values underestimate the actual effect size because some of the imaged axons may not have been fully or not at all stimulated by the HFS, yet they were included in the analysis (*SI Appendix*, Fig. S5). In line with this, a sizeable fraction (>20%) of axon segments showed much larger increases in diameter (>10%, corresponding to a ~21% increase in cross-sectional area), whereas others appeared not to undergo any structural changes at all (*SI Appendix*, Fig. S6).

We applied (2R)-amino-5-phosphonovaleric acid (APV) to test whether these structural effects depended on NMDA receptor activation. Although they were prevented on the long-term [at 45 min: bouton size: +1.4 ± 1.3% ($n = 109$ boutons; $P = 0.95$); axon diameters: +2.1 ± 0.6% ($P = 0.28$; $n = 317$ 1-μm-long shaft segments); Fig. 3 *B* and *C*] and LTP was blocked (30-40 min after HFS, $P > 0.18$; $n = 8$ slices; Fig. 3*D*), the initial enlargement of synaptic boutons was not blocked by the drug (at 2 min: +21.9 ± 2.8%; $P < 0.001$; $n = 148$ boutons; Fig. 2*B*).

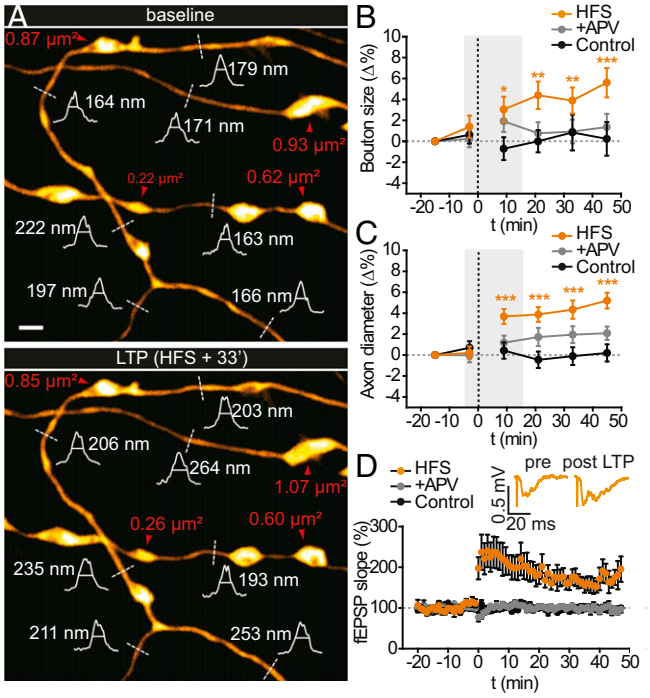

Fig. 3. STED imaging of long-term dynamics of synaptic boutons and axon diameters. (*A*) Synaptic boutons (red arrowheads) remained slightly enlarged, and axon diameters (white curve, intensity profiles; dashed lines, FWHM) grew wider relative to pre-HFS baseline levels. (*B* and *C*) Quantification of late morphological changes. (*B*) Normalized synaptic bouton sizes for HFS, control, and APV conditions. (*C*) Normalized axon diameters for these conditions. The gray boxes in *B* and *C* correspond to the time window of the short-term experiments in Fig. 2. (*D*) Normalized time course of the fEPSP slope during LTP induction. Inset shows representative fEPSP traces. LTP was blocked by APV, and the recordings were stable under control conditions. (Scale bar, 1 μm.)

In addition, we also used a more physiological pattern of hippocampal activity (theta-burst stimulation) as a current injection protocol in whole-cell patch-clamp mode. Theta-burst stimulation-induced patterns of AP firing in the CA3 neurons led to similar morphological effects on CA3 boutons and axon diameters, in terms of both direction and time course (*SI Appendix*, Fig. S7).

Mathematical Modeling Predicts Functional Consequences of Morphological Plasticity. Given the influence of axon diameter on the axial resistance of axons, we wondered whether these morphological changes might affect AP conduction velocity. To explore this possibility, we used compartmental modeling to simulate AP propagation along unmyelinated axons as a function of morphological changes in boutons and axon shafts.

Increasing axon diameters accelerated AP conduction along the axons in the model (Fig. 4 *A* and *C* and *SI Appendix*, Fig. S8), which is in line with cable theory (6, 7). Wider axons have less internal electrical resistance, and thus longer space constants, which effectively facilitates the electrotonic spread of the AP. Interestingly, enlarging synaptic boutons affected AP conduction velocity in exactly the opposite way (Fig. 4 *B* and *C*). This effect can be explained biophysically by the extra time it takes for propagating APs to charge up membranes of enlarged synaptic boutons. For axon shafts, the axial resistance is inversely proportional to the square of the radius ($\sim 1/r^2$), whereas the capacitance of the axon scales linearly with radius ($\sim r$), explaining why the accelerating effect on AP conduction wins out in the axon shafts. In contrast, changes in bouton size mostly affect the capacitance of the boutons and, to a much lesser extent, the axial resistance of the axons, which accounts for the slowing down effect predicted by the simulations.

In contrast to the effects on conduction velocity, the waveform of the AP was barely affected by any changes in morphology (*SI Appendix*, Fig. S9). This is probably because of the local regenerative nature of the AP, which acts as a reset that counteracts any potential build-up of changes in AP waveform during AP propagation. Moreover, the simulation results did not depend on whether the number or density of voltage-gated Na^+ and K^+ channels were kept constant (*SI Appendix*, Fig. S10).

We then simulated AP propagation based on the time course and magnitude of the morphological changes we experimentally observed in the axons (Fig. 4*D*). The simulations predict biphasic effects on AP conduction velocity, showing an initial increase in AP conduction delay followed by a sustained reduction (Fig. 4*E*).

To estimate the cumulative effects on AP propagation by changes in conduction speed along the axon, we calculated the changes in conduction latency as a function of axon length, which can be more than 22 mm for Schaffer collateral axons (14). As thin unmyelinated fibers conduct APs rather slowly (< 0.2 m/s) (15), the cumulative changes in latency grew into the range of several milliseconds over relatively short AP travel distances (< 10 mm; Fig. 4 *F* and *G*). Depending on whether the structural changes affected the boutons or axon shafts, the latency either increased or decreased. Notably, the magnitude of the structural changes where the simulated delays became sizable was within the experimentally observed range.

Electrophysiological Test of Functional Predictions. To test the model predictions on AP conduction velocity, we performed electrophysiological measurements. We measured AP latency in response to antidromic stimulation of CA3 afferents by whole-cell patch-clamp recordings (Fig. 5*A*) before and after application of the HFS protocol. In parallel, we recorded field potentials in CA1 *stratum radiatum* to confirm successful LTP induction. We checked that the latency measurements were not contaminated by synaptic responses by blocking glutamatergic transmission (*SI Appendix*, Fig. S11), which silenced excitatory

NEUROSCIENCE

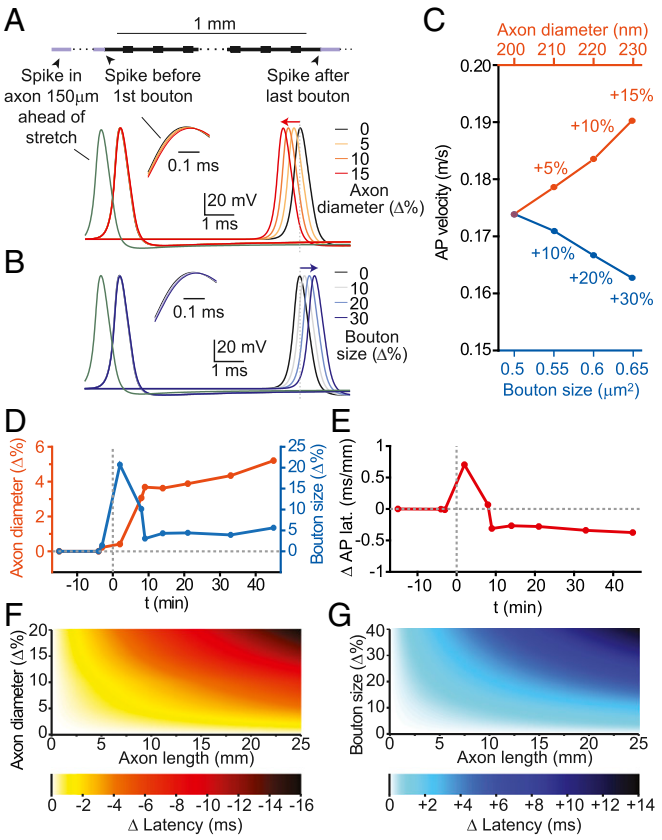

Fig. 4. Mathematical modeling of morphological effects on AP propagation. (*A*) Increasing the diameter of the axon speeds up AP conduction, whereas (*B*) increasing bouton size slows it down, according to numerical simulations of AP propagation based on a geometrically constructed model axon [axon length = 1 mm; axon shaft diameter = 200 nm; synaptic boutons (size = width × length = 0.5 × 1.0 µm) spaced every 3 µm]. (*C*) Conduction velocity as a function of bouton size and axon shaft diameter. (*D*) Time course of measured changes in axon diameters (orange; left *y* axis) and bouton sizes (blue; right *y* axis) used for morphologically realistic numerical simulations. (*E*) Morphological changes exert biphasic effect on AP latency, according to numerical simulations based on STED morphological data, expressed as latency change (in milliseconds) per axon length (in millimeters). (*F* and *G*) Color-coded plots showing the change in AP latency as a function of axon length and percentage increases of axon diameter (*F*) or bouton size (*G*).

field potentials (fEPSPs) in the CA1 area, but not the antidromic responses in the CA3 neurons (Fig. 5*B*). Although AP latency was highly reproducible for a given neuron, it varied substantially across different neurons (CV_{within} = 1.8 ± 0.1%; CV_{across} = 30.5%; $P < 0.001$; $n = 29$ cells from 29 slices; one-sample *t* test; Fig. 5 *C* and *D*).

Immediately after HFS, antidromic responses in CA3 pyramidal neurons were substantially delayed (range = −92 to +562 µs; +3.3 ± 1.5%; $P < 0.025$, $n = 10$ cells; one-tailed paired *t* test, Fig. 5 *E* and *F*). However, AP latency was increased only for a few minutes and then decreased below baseline levels 15 min after HFS, until the end of the ∼45 min of recordings (range = −326 to +29 µs; −2.2 ± 0.77% at 30–40 min; $P < 0.02$; $n = 10$ cells; Fig. 5*F*). At the same time, LTP was robustly expressed throughout this period (+81 ± 22%; $P < 0.006$; $n = 10$ slices; two-sample *t* test; Fig. 5*G*). Applying APV, we also observed an initial increase in AP latency right after HFS, but did not observe any delayed decrease (range = −49 to +60 µs; −0.12 ± 0.42%; $n = 8$ cells; $P > 0.28$; Fig. 5 *F* and *H*), mirroring the effects of APV on the time course of the morphological changes.

This qualitative agreement between the model predictions (Fig. 4*E*) and the direction and time course of the electrophysiological changes (Fig. 5*F*) supports the view that the effects on AP latency were, at least in part, caused by the activity-induced changes in axonal morphology, likely reflecting a biophysical consequence of an altered electrotonic structure of the axon. As the electrophysiological responses were measured over relatively short distances (<1 mm), the observed changes in conduction delay were accordingly small (<0.5 ms).

Discussion

Our study outlines a form of activity-dependent morphological plasticity of axonal fibers, which is associated with changes in spike velocity, and thus may influence the timing of information transfer in neural circuits. In contrast, other forms of structural plasticity, such as spine enlargement after LTP, are primarily thought of in terms of influencing the amplitude, but not the timing of synaptic signals.

Although activity-dependent changes in AP conduction velocity and synaptic delay have been reported before (16–19), their underlying mechanisms have remained elusive. On the basis of STED imaging in living brain tissue, we present evidence for activity-driven changes in presynaptic boutons and axon shafts that

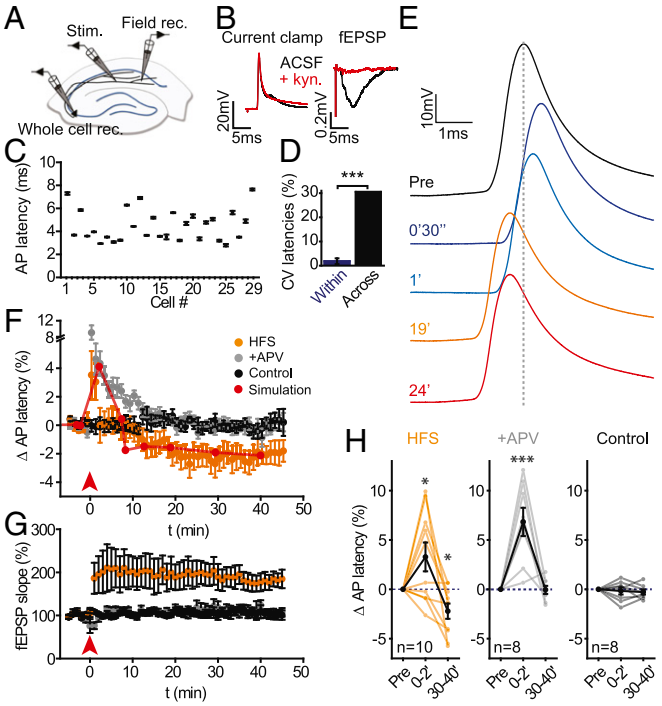

Fig. 5. Activity-dependent changes in AP conduction delay. (*A*) Recording configuration for measuring antidromic AP latency of CA3 pyramidal neurons. Field rec., fEPSP recording; Stim., stimulation electrode; Whole cell rec., whole-cell recording. (*B*) Antidromic AP waveform recorded in current clamp at the soma. Blocking glutamatergic transmission with 2 mM kynurenate (kyn) did not prevent APs generated by direct stimulation (red). (*C*) Axonal AP latencies measured from 29 CA3 pyramidal neurons (average of 20 AP latencies during a 5-min period). (*D*) Coefficient of variation of AP latencies within and across cells. (*E*) Change in AP latency induced by HFS. (*F*) AP latency transiently increased after HFS (orange, arrow indicates stimulation), but decreased to below baseline levels (black) 10 min after HFS. APV spared the early increase in AP latency, but blocked its sustained reduction later on (gray). Continuous red line shows time course of AP latency changes predicted by model simulations based on STED data (Fig. 4*D*). (*G*) Time course of the fEPSP slope for the three groups. LTP was not induced in the presence of APV. The recordings were stable under control conditions. (*H*) Paired comparisons to baseline of early and late changes in AP latency for the three groups.

were accompanied by bidirectional changes in AP conduction delay. Presynaptic boutons enlarged mostly transiently, whereas axon diameters increased in a gradual and sustained way after firing a high-frequency train of APs. These effects were observed for two different types of stimulation protocols (HFS and theta-burst stimulation) and recording configurations (extracellular field and single-cell recordings). Numerical simulations of AP propagation incorporating the morphological data based on live STED imaging could account well for the observed functional changes. In addition to acute changes in morphology, static differences between individual axons, which may reflect their plasticity history, are likely to contribute to the dispersion of AP conduction delays.

Conceivably, other processes may also have contributed to the changes in AP conduction; for example, changes in the distribution or properties of voltage-gated conductances, affecting the kinetics of the AP (active voltage spread), or changes in the number and location of organelles inside the axons, such as transport packets or mitochondria, which could influence the space constant of the axon (passive voltage spread).

Pioneering work more than 40 years ago provided the first evidence for microscopic swelling of axons during firing of APs (20, 21), leading to changes in light reflectivity of brain tissue in response to neuronal activity (22, 23). These changes reflect transient osmotic effects caused by the flow of ions and water molecules across the axolemma during AP depolarization and repolarization, where the axonal volume typically recovers quickly after the end of AP firing. In contrast, the morphological changes we documented here showed a very different time course, where most of the bouton enlargement was over after several minutes, whereas the axon diameter increase developed gradually and persisted for at least 45 min. Moreover, Cd^{2+} blocked the bouton enlargement, even though the axon still fired the same number of APs, whereas APV blocked the long-term changes in axon shaft diameter, further distinguishing our observations from previous reports of axonal swelling.

Potential Mechanisms Underlying Axon Enlargement. What physical mechanisms could account for the size increases? Physical stretching of the axolemma is unlikely to contribute much to the observed size increases because biological membranes exhibit modest elastic properties (24). In contrast, rapid redistribution and/or de novo synthesis of membrane are more likely to provide the source of the activity-dependent net enlargement of the axons.

The time course of the morphological changes suggests a scenario whereby a massive exocytosis of neurotransmitter vesicles induced by strong AP firing caused an initial increase in bouton size, which in turn led to delayed widening of the axons as some of the newly added membrane diffused away from the boutons to the adjacent axon shafts.

The pharmacological experiments support this hypothesis because Cd^{2+}, which blocks synaptic release, abolished the initial enlargement of the boutons, whereas APV did not affect the bouton changes. In contrast, APV blocked the long-term morphological and functional effects, indicating that their consolidation requires NMDA receptor/Ca^{2+}-signaling. Moreover, a recent electron microscopy study showed NMDAR-dependent long-term depletion of axonal vesicles after LTP induction (25).

The axonal swelling may also reflect an increase in the number of transport vesicles in the axon that have been shown to replenish the synaptic vesicle pool (26) or to deliver protein material to nascent synapses (27). However, the addition of such vesicles would make the intra-axonal space more crowded, and thus counteract the effect of axonal widening on AP conduction velocity.

Functional Effect on Neural Circuits. Changes in AP conduction latency may affect several important aspects of hippocampal and cortical physiology, which are sensitive to (sub)millisecond timing variations. They may be important for spike-timing dependent plasticity, as the time window for supralinear summation of calcium caused by dendritic spikes and synaptic events is on the order of a few milliseconds and determines whether synapses get potentiated or depressed (28). A change in the exact time of arrival of excitatory inputs may also affect the dynamic balance of excitatory and inhibitory drive, which controls postsynaptic spiking (29) and network oscillations (30). Because the effects scale with axon length, the transfer of information to distant targets via long-range fibers may be particularly affected by changes in spike velocity, shaping the correlation and integration time constants for neuronal activity across different brain areas (31). Although these speculations apply in general to positive and negative changes in conduction delay, their directionality, in addition to their magnitude, may very well determine the nature and extent of the downstream functional consequences.

The morphological changes may also affect the fidelity of AP conduction by changing the electrical impedance at axon branch points, where AP propagation failures might occur (32–35). In addition to these electrical effects, changes in axon diameter may influence the spread of signaling molecules along the axon, imposing a variable diffusion barrier that could regulate the degree of biochemical compartmentalization of presynaptic boutons, akin to the situation for the neck of dendritic spines (36). Finally, the morphological changes may perturb the structural integrity of the boutons and the nanodomains that underlie tight excitation-release coupling; for example, by altering the spatiotemporal profile of presynaptic Ca^{2+} transients or the access of the vesicular pool to the active zone, which may affect synaptic release probability or short-term plasticity.

Methods

Organotypic Hippocampal Slice Cultures. Organotypic hippocampal slices (Gähwiler type) were dissected from 5–7-d-old wild-type mice and cultured 3–5 wk in a roller drum at 35 °C, as previously described (37). Experimental procedures were in accordance with the European Union and CNRS UMR 5297 institutional guidelines for the care and use of laboratory animals (Council directive 2010/63/EU) and approved by the Committee of Ethics of Bordeaux (no. 50120198-A).

Electrophysiology. fEPSPs were recorded from the CA1 *stratum radiatum*, using glass microelectrodes (tip resistance, 3–5 MΩ) filled with artificial cerebrospinal fluid (ACSF). To increase the overlap between the labeled and stimulated fibers, a monopolar stimulating electrode (3-5 MΩ filled with ACSF) was placed in the center of the labeled CA3 cell bodies. Brief current pulses (0.2 ms) were delivered from a stimulus isolator (AMPI; Science Products). Stimulus strength (ranging between 10 and 35 μA) was adjusted to elicit fEPSPs at 50% of their maximal amplitude. fEPSPs were recorded using a patch clamp amplifier (Multiclamp 700B; Molecular Devices) with a gain of 20× and a Bessel filter set at 2 kHz. A test pulse was recorded every 15 s throughout the recordings. The stimulus protocol consisted of three trains of 100 pulses delivered at 100 Hz and 20 s apart to induce LTP and was started after recording a baseline of 20 min. The initial slopes of the fEPSPs were determined with Clampfit 10.1 (Molecular Devices). CA3 pyramidal neurons were recorded in current clamp mode with a dynamic current injection correction to maintain the resting membrane at −70 mV. The gain of the patch clamp amplifier was set at 1×, and a Bessel filter with a cutoff frequency of 2 kHz was applied. The data were digitized at a sampling rate of 250 kHz. To elicit antidromic APs, a glass electrode back-filled with ACSF was positioned in the distal part of the CA1 area, and brief current pulses (0.1 ms, 25–75 μA) were delivered from a stimulus isolator. The electrode was moved toward the CA3 area until an antidromic AP could be recorded reliably at the soma. Recordings with access resistances larger than 25 MΩ or holding currents greater than −100 pA were excluded from the analysis. fEPSP recordings in the CA1 *stratum radiatum* were performed concurrently, using the same stimulation electrode.

STED Microscopy. We used a home-built STED microscope based on an inverted microscope (DMI 6000 CS Trino; Leica), using a galvanometric beam scanner (Yanus IV; TILL Photonics) and a high numerical aperture objective lens (PL APO, 100×, oil, NA 1.4; Leica), as described in detail previously (38).

Image Acquisition. Image acquisition was controlled by the software Imspector (A. Schönle, MPI for Biophysical Chemistry). Image acquisition parameters were chosen to minimize photodamage and photobleaching. All images were acquired with time-averaged powers of <6 μW for excitation and <8 mW for STED (measured at the back aperture of the objective). Image stacks were acquired with a voxel size of 19.5 nm (xy), 375 nm (z) and a dwell time of 15 μs (*SI Appendix*, Fig. S12). The imaging depth was controlled by a piezo z-focusing device (Physikinstrumente) and was maximally 15 μm below tissue surface. For the short-term experiments, z-stacks of 40 × 40 × 3 μm (x, y, and z) were acquired every 6 min, whereas for the long-term experiments, z-stacks of 30 × 20 × 3 μm were acquired every 12 min for 1 h, where two image stacks were acquired before the stimulus and four image stacks afterward.

Image Analysis. We used NIH ImageJ and Matlab scripts for image processing and analysis. Analysis was done on raw data, whereas a one-pixel median filter was applied to the images shown in the figures. A maximum-intensity projection was applied on identified axon segments. To perform automated measurements, a reference image that consisted of a line of pixels running along the axon segment was produced by thresholding and binarizing the images before using a skeletonization plugin from ImageJ. The full width at half maximum (FWHM) was measured automatically along the axon guided by the reference image. For every position, intensity profiles from three parallel lines were averaged to reduce noise. Diameter profiles of full axon segments were generated and analyzed further (*SI Appendix*, Fig. S2). To determine bouton size changes over time, bouton area was calculated as the integral of the local diameter profile. Similarly, axon shaft diameter changes were calculated as the local average axon shaft diameter from each 1-μm segment. For each field stimulation experiment, approximately six axon segments were analyzed with a total axon shaft length of around 25 μm and 20 synaptic boutons. Instances of bouton turnover were excluded from this analysis. The gain and loss of boutons was analyzed separately (*SI Appendix*, Fig. S13).

Numerical Simulations. The propagation of APs along unmyelinated axons was simulated using the simulation environment NEURON [version 7.3 (39)]. Two different kinds of compartmental models were used to analyze how axon morphology influences AP conduction velocity. The first model was a geometrically constructed using average characteristics of CA3 axons (axon shaft diameter = 200 nm; presynaptic boutons = 1 μm long and 0.5 μm wide, spaced every 3 μm along the axon), whereas the second one was based on a realistic morphological reconstruction (using STED data). The multicompartment model used standard channel kinetic equations (40), using published parameters for hippocampal pyramidal neurons (41, 42) (*SI Appendix*).

ACKNOWLEDGMENTS. We thank A. Penn for the Sindbis-GFP virus and T. Mrsic-Flögel and D. DiGregorio for comments on the manuscript. The confocal images of fixed samples were taken in the Bordeaux Imaging Center, a service unit of the Centre National de la Recherche Scientifique, Institut national de la santé et de la recherche médicale, and the University of Bordeaux and member of France BioImaging. The study was supported by Fondation pour la Recherche Médicale, Initiative d'excellence de l'Université de Bordeaux, Agence nationale de la recherche (SUPERTri, ANR-13-BSV4-0007-01), LabEx BRAIN, France-BioImaging (ANR-10-INSB-04), and European Research Area Network NEURON II (ANR-12-NEUR-0007-03).

1. Debanne D, Campanac E, Bialowas A, Carlier E, Alcaraz G (2011) Axon physiology. *Physiol Rev* 91(2):555–602.
2. Alle H, Geiger JR (2006) Combined analog and action potential coding in hippocampal mossy fibers. *Science* 311(5765):1290–1293.
3. Grubb MS, Burrone J (2010) Activity-dependent relocation of the axon initial segment fine-tunes neuronal excitability. *Nature* 465(7301):1070–1074.
4. Becker N, Wierenga CJ, Fonseca R, Bonhoeffer T, Nägerl UV (2008) LTD induction causes morphological changes of presynaptic boutons and reduces their contacts with spines. *Neuron* 60(4):590–597.
5. Sasaki T, Matsuki N, Ikegaya Y (2011) Action-potential modulation during axonal conduction. *Science* 331(6017):599–601.
6. Goldstein SS, Rall W (1974) Changes of action potential shape and velocity for changing core conductor geometry. *Biophys J* 14(10):731–757.
7. Waxman SG, Bennett MV (1972) Relative conduction velocities of small myelinated and non-myelinated fibres in the central nervous system. *Nat New Biol* 238(85): 217–219.
8. Greenberg MM, Leitao C, Trogadis J, Stevens JK (1990) Irregular geometries in normal unmyelinated axons: A 3D serial EM analysis. *J Neurocytol* 19(6):978–988.
9. Wang SS, et al. (2008) Functional trade-offs in white matter axonal scaling. *J Neurosci* 28(15):4047–4056.
10. Shepherd GM, Harris KM (1998) Three-dimensional structure and composition of CA3–>CA1 axons in rat hippocampal slices: Implications for presynaptic connectivity and compartmentalization. *J Neurosci* 18(20):8300–8310.
11. Westrum LE, Blackstad TW (1962) An electron microscopic study of the stratum radiatum of the rat hippocampus (regio superior, CA 1) with particular emphasis on synaptology. *J Comp Neurol* 119:281–309.
12. Bastrikova N, Gardner GA, Reece JM, Jeromin A, Dudek SM (2008) Synapse elimination accompanies functional plasticity in hippocampal neurons. *Proc Natl Acad Sci USA* 105(8):3123–3127.
13. Haber M, Vautrin S, Fry EJ, Murai KK (2009) Subtype-specific oligodendrocyte dynamics in organotypic culture. *Glia* 57(9):1000–1013.
14. Wittner L, Henze DA, Záborszky L, Buzsáki G (2007) Three-dimensional reconstruction of the axon arbor of a CA3 pyramidal cell recorded and filled in vivo. *Brain Struct Funct* 212(1):75–83.
15. Meeks JP, Mennerick S (2007) Action potential initiation and propagation in CA3 pyramidal axons. *J Neurophysiol* 97(5):3460–3472.
16. Bakkum DJ, Chao ZC, Potter SM (2008) Long-term activity-dependent plasticity of action potential propagation delay and amplitude in cortical networks. *PLoS One* 3(5):e2088.
17. Boudkkazi S, et al. (2007) Release-dependent variations in synaptic latency: A putative code for short- and long-term synaptic dynamics. *Neuron* 56(6):1048–1060.
18. Chida K, Kaneko K, Fujii S, Yamazaki Y (2015) Activity-dependent modulation of the axonal conduction of action potentials along rat hippocampal mossy fibers. *Eur J Neurosci* 41(1):45–54.
19. Voronin LL, Volgushev M, Chistiakova M, Kuhnt U, Singer W (1996) Involvement of silent synapses in the induction of long-term potentiation and long-term depression in neocortical and hippocampal neurons. *Neuroscience* 74(2):323–330.
20. Cohen LB (1973) Changes in neuron structure during action potential propagation and synaptic transmission. *Physiol Rev* 53(2):373–418.
21. Iwasa K, Tasaki I, Gibbons RC (1980) Swelling of nerve fibers associated with action potentials. *Science* 210(4467):338–339.
22. Fields RD (2011) Signaling by neuronal swelling. *Sci Signal* 4(155):tr1.
23. Vincis R, Lagier S, Van De Ville D, Rodriguez I, Carleton A (2015) Sensory-evoked intrinsic imaging signals in the olfactory bulb are independent of neurovascular coupling. *Cell Reports* 12(2):313–325.
24. Diz-Muñoz A, Fletcher DA, Weiner OD (2013) Use the force: Membrane tension as an organizer of cell shape and motility. *Trends Cell Biol* 23(2):47–53.
25. Bourne JN, Chirillo MA, Harris KM (2013) Presynaptic ultrastructural plasticity along CA3→CA1 axons during long-term potentiation in mature hippocampus. *J Comp Neurol* 521(17):3898–3912.
26. Staras K, et al. (2010) A vesicle superpool spans multiple presynaptic terminals in hippocampal neurons. *Neuron* 66(1):37–44.
27. Ahmari SE, Buchanan J, Smith SJ (2000) Assembly of presynaptic active zones from cytoplasmic transport packets. *Nat Neurosci* 3(5):445–451.
28. Feldman DE (2012) The spike-timing dependence of plasticity. *Neuron* 75(4):556–571.
29. Xue M, Atallah BV, Scanziani M (2014) Equalizing excitation-inhibition ratios across visual cortical neurons. *Nature* 511(7511):596–600.
30. Buzsáki G, Draguhn A (2004) Neuronal oscillations in cortical networks. *Science* 304(5679):1926–1929.
31. Izhikevich EM (2006) Polychronization: Computation with spikes. *Neural Comput* 18(2):245–282.
32. Debanne D, Guérineau NC, Gähwiler BH, Thompson SM (1997) Action-potential propagation gated by an axonal I(A)-like K+ conductance in hippocampus. *Nature* 389(6648):286–289.
33. Lüscher C, Streit J, Lipp P, Lüscher HR (1994) Action potential propagation through embryonic dorsal root ganglion cells in culture. II. Decrease of conduction reliability during repetitive stimulation. *J Neurophysiol* 72(2):634–643.
34. Meeks JP, Mennerick S (2004) Selective effects of potassium elevations on glutamate signaling and action potential conduction in hippocampus. *J Neurosci* 24(1):197–206.
35. Soleng AF, Chiu K, Raastad M (2003) Unmyelinated axons in the rat hippocampus hyperpolarize and activate an H current when spike frequency exceeds 1 Hz. *J Physiol* 552(Pt 2):459–470.
36. Tønnesen J, Katona G, Rózsa B, Nägerl UV (2014) Spine neck plasticity regulates compartmentalization of synapses. *Nat Neurosci* 17(5):678–685.
37. Gähwiler BH (1981) Organotypic monolayer cultures of nervous tissue. *J Neurosci Methods* 4(4):329–342.
38. Tønnesen J, Nadrigny F, Willig KI, Wedlich-Söldner R, Nägerl UV (2011) Two-color STED microscopy of living synapses using a single laser-beam pair. *Biophys J* 101(10):2545–2552.
39. Carnevale NT, Hines ML, eds (2006) *The NEURON Book* (Cambridge University Press, Cambridge, UK).
40. Hodgkin AL, Huxley AF (1952) Propagation of electrical signals along giant nerve fibers. *Proc R Soc Lond B Biol Sci* 140(899):177–183.
41. Conde-Sousa E, Aguiar P (2013) A working memory model for serial order that stores information in the intrinsic excitability properties of neurons. *J Comput Neurosci* 35(2):187–199.
42. Traub RD, Miles R (1991) Multiple modes of neuronal population activity emerge after modifying specific synapses in a model of the CA3 region of the hippocampus. *Ann N Y Acad Sci* 627:277–290.